



Continuum thermodynamics of ferroelectric domain evolution: Theory, finite element implementation, and application to domain wall pinning

Yu Su, Chad M. Landis*

Department of Mechanical Engineering and Materials Science, MS 321, Rice University, P.O. Box 1892, Houston, TX 77251-1892, USA

Received 18 April 2006; received in revised form 11 July 2006; accepted 17 July 2006

Abstract

A continuum thermodynamics framework is devised to model the evolution of ferroelectric domain structures. The theory falls into the class of phase-field or diffuse-interface modeling approaches. Here a set of micro-forces and governing balance laws are postulated and applied within the second law of thermodynamics to identify the appropriate material constitutive relationships. The approach is shown to yield the commonly accepted Ginzburg–Landau equation for the evolution of the polarization order parameter. Within the theory a form for the free energy is postulated that can be applied to fit the general elastic, piezoelectric and dielectric properties of a ferroelectric material near its spontaneously polarized state. Thereafter, a principle of virtual work is specified for the theory and is implemented to devise a finite element formulation. The theory and numerical methods are used to investigate the fields near straight 180° and 90° domain walls and to determine the electromechanical pinning strength of an array of line charges on 180° and 90° domain walls.

© 2006 Elsevier Ltd. All rights reserved.

Keywords: Ferroelectrics; Phase-field modeling; Finite element methods; Piezoelectrics; Domain switching

*Corresponding author. Tel.: +713 348 3609; fax: +713 348 5423.

E-mail address: landis@rice.edu (C.M. Landis).

1. Introduction

Ferroelectric ceramics are being increasingly used in macro- and micro-device applications for actuators, sensors, and information storage. The fundamental behavior utilized in these devices is the strong electro-mechanical coupling exhibited by the ferroelectric material. In order to predict the performance and reliability of such devices it is necessary to understand the mechanics and physics governing the constitutive response of the ferroelectric material at the appropriate scales. The primary mechanism responsible for nonlinear ferroelectric constitutive response at practically all scales is the motion of domain walls. There is also evidence that the attractive “linear” properties of many ferroelectrics, such as high piezoelectric constants and large dielectric constants, is due to anelastic domain wall motion (Xu et al., 2005). The nature of domain walls and their interactions with other material defects is fundamental to the understanding of the physical phenomena associated with the finite coercive strength of ferroelectrics, fracture toughening associated with domain switching (Wang and Landis, 2004), and electrical fatigue associated with pinning of domain walls by migrating charge carriers (Warren et al., 1994; Xiao et al., 2005).

In this paper, a continuum thermodynamics framework is presented to model the evolution of ferroelectric domain structures. The theory falls into the class of phase-field or diffuse-interface modeling approaches (Cao and Cross, 1991; Nambu and Sagala, 1994; Hu and Chen, 1997; Ahluwalia and Cao, 2000, 2001; Li et al., 2001, 2002; Wang et al., 2004; Zhang and Bhattacharya, 2005a, b), which has the potential to bridge atomistic calculations (Cohen and Krakauer, 1992; Meyer and Vanderbilt, 2002) and the larger scale phenomenological modeling approaches. In a departure from previous derivations of the phase-field equations, a set of micro-forces and governing balance laws are postulated and applied within the second law of thermodynamics to identify the appropriate material constitutive relationships (Fried and Gurtin, 1993, 1994; Gurtin, 1996). The approach is shown to yield the commonly accepted Ginzburg–Landau equation for the evolution of the electrical polarization order parameter. Within the theory a form for the free energy is postulated that can be applied to fit the general elastic, piezoelectric, and dielectric properties of a ferroelectric material near its spontaneously polarized state. To investigate the consequences of the theory simple planar domain wall motions are analyzed. Thereafter, a principle of virtual work is specified for the theory and is implemented to devise a finite element formulation. The theory and numerical methods are used to investigate the interactions of 180° and 90° domain walls with arrays of charged defects and to determine how strongly domain walls are electromechanically pinned by the arrays of defects.

The outline of the remainder of the paper is as follows. In Section 2 the governing equations for the theory are presented, including a new micro-force balance and the consequences associated with the second law of thermodynamics. In Section 3 some analytical results associated with straight domain walls are given along with numerical results for the fields near 180° and 90° domain walls for material parameters that model BaTiO_3 . Section 4 develops a finite element formulation that can be used to numerically solve the model equations in higher dimensions. Section 5 formulates the problem of a domain wall interacting with an array of uniformly spaced line charges. Numerical finite element results are presented for the equilibrium domain wall shapes near the array and for the critical sets of electromechanical fields required to break through the array. The results

are discussed within the context of the coercive electromechanical “strength” of single crystals. Finally, Section 6 offers a discussion of the model and future avenues of study.

2. Theory

If one is given a static domain structure then the equations governing the distributions of electromechanical fields in the material based on linear piezoelectricity are well established, and there exists several numerical techniques that can be applied to solve for these fields (Allik and Hughes, 1970; Landis, 2002a). However, we are not only interested in the distribution of the fields, but also in how these fields cause the domain structure to evolve. Hence, this problem falls into a broader class of free boundary problems where the locations of the interfaces must also be determined as part of the solution. A sharp interface approach could be applied, but contains physical questions associated with special rules for nucleation, and numerical concerns associated with changes in topology of the domain structure. In order to circumvent the challenges associated with a sharp interface approach, a diffuse-interface or “phase-field” methodology is taken here.

Traditionally, the phase-field equations governing the evolution of domain configurations have been derived from a simple and physically justifiable set of assumptions. While this approach is certainly sound, it obscures the modern continuum physics distinction between fundamental balance laws, which are applicable to a wide range of materials, and the constitutive equations that are valid for a specific material (Fried and Gurtin, 1993, 1994; Gurtin, 1996). Here we present a small deformation non-equilibrium thermodynamics framework for ferroelectric domain evolution. We begin with the fundamental equations governing the electromechanical fields under the assumption of small deformations and rotations. Note that the small deformation assumption is prevalent throughout the phase-field modeling literature. The analysis of large deformations would introduce the concept of Maxwell stresses (Toupin, 1956; McMeeking and Landis, 2005), which are assumed to be higher order effects that can be neglected. Following previous phase-field modeling approaches, the effects of large deformations will not be considered here, but their incorporation within the theory is possible. It will also be assumed that the fields vary slowly with respect to the speed of light in the material, i.e. the quasi-static electromagnetic field approximation, but not necessarily with respect to the speed of sound, i.e. inertial effects are considered within the general derivation. Specifically, balances of linear and angular momentum in any arbitrary volume V and its bounding surfaces S yield

$$\sigma_{ji,j} + b_i = \rho \ddot{u}_i \quad \text{in } V, \quad (2.1)$$

$$\sigma_{ij} = \sigma_{ji} \quad \text{in } V, \quad (2.2)$$

$$\sigma_{ji} n_j = t_i \quad \text{on } S, \quad (2.3)$$

where σ_{ij} are the Cartesian components of the Cauchy stress, b_i the components of a body force per unit volume, ρ the mass density, u_i the mechanical displacements, n_i the components of a unit vector normal to a surface element, and t_i the tractions applied to the surface. Standard index notation is used with summation implied over repeated indices, the double overdot represents a second derivative with respect to time, and the subscript, j represents partial differentiation with respect to the x_j coordinate direction. Under the

assumptions of linear kinematics, the strain components ε_{ij} are related to the displacements as

$$\varepsilon_{ij} = \frac{1}{2}(u_{i,j} + u_{j,i}) \quad \text{in } V. \tag{2.4}$$

The electrical quantities of electric field, E_i ; electric potential, ϕ ; electric displacement, D_i ; volume charge density, q ; and surface charge density, ω ; are governed by the quasi-static forms of Maxwell’s equations. Specifically, in any arbitrary volume V (including a region of free space) and its bounding surface S ,

$$D_{i,i} - q = 0 \quad \text{in } V, \tag{2.5}$$

$$D_i n_i = -\omega \quad \text{on } S, \tag{2.6}$$

$$E_i = -\phi_{,i} \quad \text{in } V. \tag{2.7}$$

Within the theory of linear piezoelectricity, Eqs. (2.1)–(2.7) represent the fundamental balance laws and kinematic relationships, and the constitutive laws required to close the loop on the equations relate the stress and electric field to the strain and electric displacement. Such constitutive relationships can be derived from thermodynamic considerations using a material free energy that depends on the components of the strain and electric displacement (Nye, 1957). However, within the phase-field modeling approach the free energy will also be required to depend on an order parameter and its gradient. Mathematically, the order parameter is used to describe the different material variant types, i.e. the spontaneous states that are possible in a crystal. For the case of ferroelectrics, the physically natural order parameter is the electrical polarization P_i . Note that the relationship between electric field, electric displacement and material polarization is given as

$$D_i = P_i + \kappa_0 E_i \quad \text{in } V. \tag{2.8}$$

Here κ_0 is the permittivity of free space. Given that the free energy will be allowed to depend on a new independent variable P_i , we must now allow for a new system of “micro-forces” that are work conjugate to this configurational quantity. Following the work (and wording) of Fried and Gurtin (1993, 1994), and Gurtin (1996) we introduce a micro-force tensor ξ_{ji} such that $\xi_{ji} n_j \dot{P}_i$ represents a power density expended across surfaces by neighboring configurations, an *internal* micro-force vector π_i such that $\pi_i \dot{P}_i$ is the power density expended by the material internally, e.g. in the ordering of atoms within unit cells of the lattice (this micro-force will account for dissipation in the material), and an external micro-force vector γ_i such that $\gamma_i \dot{P}_i$ is a power density expended on the material by external sources. Then, the integral balance of this set of configurational forces leads to the differential balance law

$$\int_S \xi_{ji} n_j dS + \int_V \pi_i dV + \int_V \gamma_i dV = 0 \Rightarrow \xi_{ji,j} + \pi_i + \gamma_i = 0 \quad \text{in } V. \tag{2.9}$$

To remain as general as possible, it is assumed that the Helmholtz free energy of the material (including the free space occupied by the material) takes the following form:

$$\psi = \psi(\varepsilon_{ij}, D_i, P_i, P_{i,j}, \dot{P}_i). \tag{2.10}$$

Note that temperature plays a key role in ferroelectric phase transitions near the Curie point. For isothermal behavior, the Helmholtz free energy remains the appropriate energy

functional with the additional complication that the material parameters of the free energy are temperature dependent (Devonshire, 1954; Jona and Shirane, 1962). Here we will deal only with constant temperature behavior below the Curie temperature, but recognize that the extension to spatially homogeneous temperature-dependent behavior can be readily included within the present framework simply by specifying the temperature at which the material properties must be evaluated. In contrast, the inclusion of spatially *inhomogeneous* temperature-dependent behavior and the associated thermal diffusion requires an analysis of the second law of thermodynamics including such effects, and would call for the introduction of temperature and entropy as additional field variables within the theory and numerical treatment. In the following, only the constant temperature cases will be considered.

For the isothermal processes below the Curie temperature under consideration, the second law of thermodynamics is written as the Clausius–Duhem (dissipation) inequality as

$$\int_V \dot{\psi} dV + \frac{d}{dt} \int_V \frac{1}{2} \rho \dot{u}_i \dot{u}_i dV \leq \int_V (b_i \dot{u}_i + \phi \dot{q} + \gamma_i \dot{P}_i) dV + \int_S (t_i \dot{u}_i + \phi \dot{\omega} + \zeta_{ji} n_j \dot{P}_i) dS. \quad (2.11)$$

Here the left-hand side represents the rate of stored plus kinetic energy in the material and the right-hand side represents the power expended by external sources on the body. Note that the internal micro-force π_i does not contribute to this external power term. Substitution into (2.11) of the balance laws of Eqs. (2.1)–(2.9), along with the application of the divergence theorem yields

$$\begin{aligned} & \int_V \frac{\partial \psi}{\partial \varepsilon_{ij}} \dot{\varepsilon}_{ij} + \frac{\partial \psi}{\partial D_i} \dot{D}_i + \frac{\partial \psi}{\partial P_i} \dot{P}_i + \frac{\partial \psi}{\partial P_{i,j}} \dot{P}_{i,j} + \frac{\partial \psi}{\partial \dot{P}_i} \ddot{P}_i dV \\ & \leq \int_V \sigma_{ji} \dot{\varepsilon}_{ij} + E_i \dot{D}_i + \zeta_{ji} \dot{P}_{i,j} - \pi_i \dot{P}_i dV. \end{aligned} \quad (2.12)$$

Note that the assumption implicit to Eq. (2.10) is that the stress, electric field, micro-force tensor, and internal micro-force each are allowed to depend on ε_{ij} , D_i , P_i , $P_{i,j}$, and \dot{P}_i . The question can be raised as to why the free energy must be allowed to depend on \dot{P}_i . The answer being that since the internal micro-force π_i is allowed to depend on \dot{P}_i , then all of the thermodynamic forces must also potentially have such dependence (Coleman and Noll, 1963). It will be shown that the second law inequality ultimately allows only π_i to depend on \dot{P}_i (see Eqs. (2.13) and (2.14)). Following Coleman and Noll (1963), it is assumed that for a given thermodynamic state, arbitrary levels of $\dot{\varepsilon}_{ij}$, \dot{D}_i , \dot{P}_i , $\dot{P}_{i,j}$, and \ddot{P}_i are permissible through the appropriate control of the external sources b_i , q , and γ_i . Then, given that Eq. (2.12) must hold for all permissible processes, an analysis of the dissipation inequality implies that

$$\frac{\partial \psi}{\partial \dot{P}_i} = 0 \Rightarrow \psi = \psi(\varepsilon_{ij}, D_i, P_i, P_{i,j}), \quad (2.13)$$

$$\sigma_{ji} = \frac{\partial \psi}{\partial \varepsilon_{ij}}, \quad E_i = \frac{\partial \psi}{\partial D_i}, \quad \text{and} \quad \zeta_{ji} = \frac{\partial \psi}{\partial P_{i,j}}. \quad (2.14)$$

Finally, after defining $\eta_i \equiv (\partial\psi/\partial P_i)$, the internal micro-force π_i must satisfy

$$\begin{aligned} (\pi_i + \eta_i) \dot{P}_i \leq 0 &\Rightarrow \pi_i = -\eta_i - \beta_{ij} \dot{P}_j \\ \text{with } \beta_{ij} = \beta_{ij}(\varepsilon_{kl}, D_k, P_k, P_{k,l}, \dot{P}_k) &\text{ positive definite.} \end{aligned} \quad (2.15)$$

If the inverse “mobility” tensor β is constant and the high-temperature phase is cubic then $\beta_{ij} = \beta\delta_{ij}$ where $\beta \geq 0$. This is the simplest and most widely applied form for β_{ij} . Substitution of Eqs. (2.14c) and (2.15) into the micro-force balance of Eq. (2.9) yields a generalized form of the Ginzburg–Landau equation governing the evolution of the material polarization in a ferroelectric material.

$$\left(\frac{\partial\psi}{\partial P_{i,j}} \right)_j - \frac{\partial\psi}{\partial P_i} + \gamma_i = \beta_{ij} \dot{P}_j \quad \text{in } V. \quad (2.16)$$

Therefore, the postulated set of micro-forces in Eq. (2.9) is justified by the fact that their existence implies the accepted form of the phase-field equations. The primary differences between the present derivation of Eq. (2.16) and the historical approach is that a set of new micro-forces is introduced, and a distinction is made between the fundamental balance laws that must be applicable to all materials and the constitutive laws that are specific to a given material.

It is important to note that the free energy introduced in Eq. (2.10) and further constrained in Eq. (2.13) includes both the energy stored in the material and the energy stored in the free space occupied by the material. This distinction becomes important when comparing to the work of other researchers, e.g. Zhang and Bhattacharya (2005a, b). Specifically, the free energy must be decomposed into the free energy of the material and the free energy of the free space such that

$$\psi(\varepsilon_{ij}, D_i, P_i, P_{i,j}) = \bar{\psi}(\varepsilon_{ij}, P_i, P_{i,j}) + \frac{1}{2\kappa_0}(D_i - P_i)(D_i - P_i). \quad (2.17)$$

Then, the material free energy $\bar{\psi}$ is analogous to $U+W$ as used by Zhang and Bhattacharya (2005a). After the application of Eqs. (2.7) and (2.8), Eq. (2.16) is a generalization of the evolution equation obtained by Zhang and Bhattacharya (2005a) who applied a gradient flow of energy technique for their derivation. Furthermore, for problems where the fields permeate into the vacuum, then $\bar{\psi} = 0$ and $P_i = 0$ in regions of free space.

We now proceed to the specification of the free energy. The goal for this task is that the general form of the free energy must contain a sufficient set of parameters such that for a given material these parameters can be fit to the spontaneous polarization, spontaneous strain, dielectric permittivity, piezoelectric coefficients and the elastic properties near the stress and electric field free spontaneous polarization and strain states. To accomplish this task we introduce the following form for the free energy:

$$\begin{aligned} \psi = & \frac{1}{2} a_{ijkl} P_{i,j} P_{k,l} + \frac{1}{2} \bar{a}_{ij} P_i P_j + \frac{1}{4} \bar{\bar{a}}_{ijkl} P_i P_j P_k P_l + \frac{1}{6} \bar{\bar{\bar{a}}}_{ijklmn} P_i P_j P_k P_l P_m P_n \\ & + \frac{1}{6} \bar{\bar{\bar{a}}}_{ijklmnrs} P_i P_j P_k P_l P_m P_n P_r P_s + b_{ijkl} \varepsilon_{ij} P_k P_l + \frac{1}{2} c_{ijkl} \varepsilon_{ij} \varepsilon_{kl} \\ & + f_{ijklmn} \varepsilon_{ij} \varepsilon_{kl} P_m P_n + g_{ijklmn} \varepsilon_{ij} P_k P_l P_m P_n + \frac{1}{2\kappa_0} (D_i - P_i)(D_i - P_i). \end{aligned} \quad (2.18)$$

First note that each of the newly introduced material tensors must contain the symmetry of the high-temperature material phase, which for most ferroelectrics of interest is cubic. The first term of the free energy penalizes large gradients of polarization and gives domain walls thickness within the model, this is also referred to as an “exchange energy”. The four terms on the second line are used to create the non-convex energy landscape of the free energy with minima located at the spontaneous polarization states. The four terms on the third line are then used to fit the material’s spontaneous strain along with the dielectric, elastic, and piezoelectric properties about the spontaneous state. Note that the elastic, dielectric, and piezoelectric properties are non-linear, and therefore the tensor components are fit to the tangent material properties at the spontaneously polarized state. The final term represents the energy stored within the free space occupied by the material, and according to Eq. (2.8) is equivalent to $\kappa_0 E_i E_i / 2$.

This form of the free energy differs from that implemented previously (Cao and Cross, 1991; Nambu and Sagala, 1994; Hu and Chen, 1997; Ahluwalia and Cao, 2000, 2001; Li et al., 2001, 2002; Wang et al., 2004; Zhang and Bhattacharya, 2005a, b) in the following ways. First, the eighth rank term on the second line was introduced by Zhang and Bhattacharya (2005a) in order to allow for adjustments of the dielectric properties and the energy barriers for 90° switching. The sixth rank terms introduced on the third line have not appeared previously in the literature and allow for the fit to the elastic, piezoelectric, and dielectric properties of the low symmetry phase in the spontaneous state. Without these terms the elastic properties of the material arise only from the c_{ijkl} tensor, which must have the symmetry of the high-temperature phase. Hence, to date, all of the phase-field models for ferroelectrics have assumed that the elastic properties of the spontaneously polarized tetragonal phase have at most cubic symmetry and several studies have assumed elastic isotropy. In many cases the simplifying assumption of cubic symmetry or isotropy has been implemented in order to simplify the numerical procedure applied for the model solution.

Along with the lack of an accurate fit to the elastic properties of the spontaneously poled phases, the free energy functionals used to date are not able to completely fit the dielectric and piezoelectric properties either. Specifically, at constant strain, the ratio of the dielectric constant perpendicular to the polarization direction to the dielectric constant parallel to the polarization direction is on the order of 40 in barium titanate (Berlincourt and Jaffe, 1958; Li et al., 1991) whereas the phase-field theories used to date to model barium titanate place this ratio at about 4. With regard to the piezoelectric coefficients, previous works use the independent components of the b_{ijkl} tensor to fit the spontaneous strain components associated with the stress and electric field free spontaneous polarization state; however, no free parameters are available to fit the piezoelectric coefficients near the spontaneous state unless the \mathbf{g} tensor is introduced. Therefore, the form of the free energy used to date can capture differences in the spontaneous polarization and strain states between BaTiO₃ and PbTiO₃, however, for either material system the elastic, piezoelectric, and dielectric properties are not accurately characterized by past models. By introducing the \mathbf{f} and \mathbf{g} tensors on the third line of Eq. (2.18), this general form of the free energy will be able to fit the magnitudes of the spontaneous polarization and strain components *and* the elastic, piezoelectric and dielectric constants near the spontaneous state. This allows for a more accurate representation and comparison of the behaviors of different material compositions.

3. Planar domain wall solutions

In this section the solutions for initially straight domain walls in the y – z plane moving at constant velocity v in the x -direction are presented. The polarization and any applied electric fields will exist in the x – y plane, i.e. $P_z = 0$ and $E_z = 0$, and generalized plane strain is assumed, i.e. $\varepsilon_{xz} = \varepsilon_{yz} = 0$ and ε_{zz} is uniform. Transforming to a coordinate system that is moving along with the domain wall at constant velocity v , symmetry considerations dictate that the solutions for stresses, strains, electric fields, electric displacements, polarizations, and micro-forces are functions of x only. Given these constraints, compatibility of strains implied by Eq. (2.4) yield

$$\varepsilon_{yy} = c_0 y + \varepsilon_{yy}^0. \tag{3.1}$$

With no free charge q , Maxwell’s laws governing the quasi-static electric displacement and the electric field distributions, Eqs. (2.5) and (2.7), imply that

$$\frac{dD_x}{dx} = 0 \Rightarrow D_x = D_x^0, \tag{3.2}$$

$$\frac{dE_y}{dx} = 0 \Rightarrow E_y = E_y^0. \tag{3.3}$$

The parameters ε_{yy}^0 , D_x^0 , and E_y^0 are the constant axial strain, electric displacement, and electric field in the associated directions. The constant c_0 arises if the domain wall is curved due to the deformation. Here only cases where the wall remains straight after the deformation will be considered and hence c_0 is taken to be zero. Then, with the fact that $\varepsilon_{xx} = \varepsilon_{xx}(x)$ and hence $u_{x,yx} = \varepsilon_{xx,y} = 0$, the momentum balances from Eq. (2.1), imply

$$\frac{d}{dx} (\sigma_{xx} - \rho v^2 \varepsilon_{xx}) = 0 \Rightarrow \sigma_{xx} = \rho v^2 \varepsilon_{xx} + \sigma_{xx}^0, \tag{3.4}$$

$$\frac{d}{dx} (\sigma_{xy} - 2\rho v^2 \varepsilon_{xy}) = 0 \Rightarrow \sigma_{xy} = 2\rho v^2 \varepsilon_{xy} + \sigma_{xy}^0, \tag{3.5}$$

where σ_{xx}^0 and σ_{xy}^0 are constants. Finally, the micro-force balances from Eq. (2.16) become

$$\frac{d\xi_{xx}}{dx} - \eta_x = -v\beta_{xx} \frac{dP_x}{dx} - v\beta_{xy} \frac{dP_y}{dx}, \tag{3.6}$$

$$\frac{d\xi_{xy}}{dx} - \eta_y = -v\beta_{yx} \frac{dP_x}{dx} - v\beta_{yy} \frac{dP_y}{dx}. \tag{3.7}$$

The solutions to Eqs. (3.1)–(3.7) are subject to the boundary conditions $\sigma_{xx}(\infty) = \sigma_{xx}^+$, $\sigma_{xx}(-\infty) = \sigma_{xx}^-$, $\sigma_{xy}(\infty) = \sigma_{xy}^+$, $\sigma_{xy}(-\infty) = \sigma_{xy}^-$, $D_x(\infty) = D_x^0$, $D_x(-\infty) = D_x^0$, $\eta_x(\infty) = 0$, $\eta_x(-\infty) = 0$, $\eta_y(\infty) = 0$, and $\eta_y(-\infty) = 0$. Along with these boundary conditions the governing equations can be solved for the electromechanical structure of a planar domain wall moving at constant velocity. Before presenting such results we first derive an expression for the Eshelby driving traction on a domain wall following the procedure of Fried and Gurtin (1994).

Sharp interface theories of domain wall dynamics require a kinetic law that describes the normal velocity of points along the interface. Such kinetic laws usually relate the normal velocity to the jump in the Eshelby energy-momentum tensor across the wall. The following derivation provides this relationship based on the diffuse interface theory. First,

multiply Eqs. (3.2) and (3.4)–(3.7) by $-E_x$, ε_{xx} , $2\varepsilon_{xy}$, $P_{x,x}$, and $P_{y,x}$ respectively. Then, defining the electrical enthalpy h as $h = \psi - E_i D_i$, the sum of these equations can be rearranged as follows:

$$\begin{aligned} \frac{d}{dx} \left(\xi_{xx} P_{x,x} + \xi_{xy} P_{y,x} + \sigma_{xx} \varepsilon_{xx} - \frac{1}{2} \rho v^2 \varepsilon_{xx}^2 + 2\sigma_{xy} \varepsilon_{xy} - 2\rho v^2 \varepsilon_{xy}^2 - E_x D_x - h \right) \\ = -v \left[\beta_{xx} P_{x,x}^2 + (\beta_{xy} + \beta_{yx}) P_{y,x} P_{x,x} + \beta_{yy} P_{y,x}^2 \right]. \end{aligned} \quad (3.8)$$

After defining $\llbracket a \rrbracket = a(\infty) - a(-\infty)$ and $\langle a \rangle = [a(\infty) + a(-\infty)]/2$, and applying the identity $\llbracket ab \rrbracket = \langle a \rangle \llbracket b \rrbracket + \langle b \rangle \llbracket a \rrbracket$, the integral of Eq. (3.8) from $x = -\infty$ to ∞ can be shown to yield

$$f \equiv \llbracket h \rrbracket - \langle \sigma_{xx} \rangle \llbracket \varepsilon_{xx} \rrbracket - 2\langle \sigma_{xy} \rangle \llbracket \varepsilon_{xy} \rrbracket + \langle D_x \rangle \llbracket E_x \rrbracket = \frac{1}{\mu} v, \quad (3.9)$$

where the Eshelby driving traction f is defined within Eq. (3.9) and the domain wall mobility μ is defined as

$$\frac{1}{\mu} = \int_{-\infty}^{\infty} \left[\beta_{xx} P_{x,x}^2 + (\beta_{xy} + \beta_{yx}) P_{x,x} P_{y,x} + \beta_{yy} P_{y,x}^2 \right] dx. \quad (3.10)$$

The left-hand side of Eq. (3.9) is the jump in Eshelby's energy–momentum tensor across a flat planar domain wall moving in the x -direction. An additional discussion of this result and its implications will be discussed later in this section. Next, numerical results for solutions to Eqs. (3.1)–(3.7) are presented.

The solutions are presented in a Cartesian coordinate system moving at constant velocity v in the x -direction. The center of the domain wall will occupy the plane $x = 0$. The material properties used for the simulations are specified in the Appendix and are representative of barium titanate. At room temperature barium titanate has a spontaneous polarization in one of the six $\langle 100 \rangle$ crystallographic directions. The low-energy domain wall configurations are those that exist in the absence of far field stresses and electric fields, i.e. walls that allow for both strain and charge compatibility across the interface (Shu and Bhattacharya, 2001). The two low-energy wall types for room temperature barium titanate are the 180° wall on a $\{100\}$ plane and the 90° domain wall on a $\{110\}$ plane.

The first sets of simulations to be presented are for stationary domain wall structures with $v = 0$. Figs. 1a and b plot the polarization and axial stress near a 180° domain wall. For these simulations the P_x , D_x , E_x , E_y , and σ_{xx} fields are equal to zero. Additionally, all of the shear stresses and the z -components of the electrical fields are also zero. For each of the simulations the out-of-plane strain is set to the spontaneous level $\varepsilon_{zz} = -0.329\varepsilon_0$, and the axial strain parallel to the domain wall, ε_{yy}^0 , is set such that the far field axial stress is $\sigma_{yy}^\infty = 0.2, 0$, or -0.2 . The characteristic length scale is $l_0 = \sqrt{a_0 P_0 / E_0}$.

Note from Fig. 1a that the application of stress increases the magnitude of the polarization far from the domain wall, and this is of course due to the piezoelectric effect. Also notice that the stresses within the domain wall are significant with the value $1.5\sigma_0 = 1$ GPa for the model properties used here for barium titanate. Also of interest is the domain wall surface energy, which is obtained from

$$\gamma_{\text{wall}} = \int_{-\infty}^{\infty} [\psi - \psi(\infty)] dx. \quad (3.11)$$

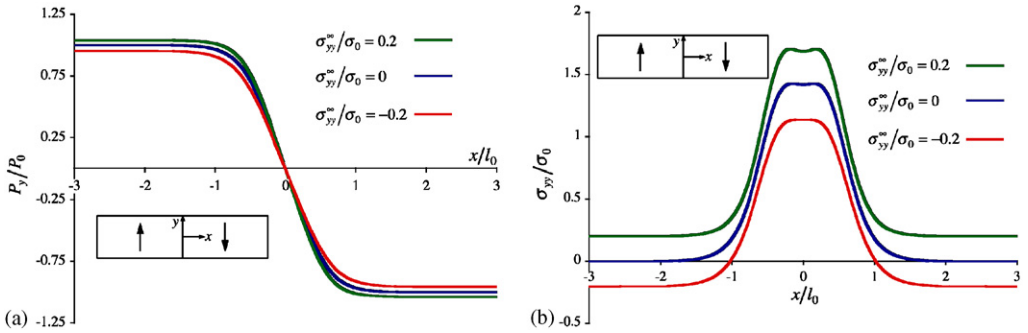


Fig. 1. (a) The polarization distribution near a stationary 180° domain wall for levels of far field applied stress of $\sigma_{yy}^\infty/\sigma_0 = -0.2, 0,$ and 0.2 . Note that the thickness of the domain wall is approximately $2l_0$, where $l_0 = \sqrt{a_0 P_0/E_0}$. (b) The axial stress distribution near a stationary 180° domain wall for levels of far field applied stress of $\sigma_{yy}^\infty/\sigma_0 = -0.2, 0,$ and 0.2 . The arrows in the small inset figures nominally represent the polarization on either side of the domain wall located at $x = 0$.

Other material parameters remaining fixed, the surface energy is directly proportional to $\sqrt{a_0}$. Taking $a_0 = 1 \times 10^{-10} \text{ V m}^3/\text{C}$, the length scale $l_0 \approx 1 \text{ nm}$, and the surface energies of these 180° domain walls are 12.6, 14.8, and 16.7 mJ/m^2 for $\sigma_{yy}^\infty/\sigma_0 = -0.2, 0,$ and 0.2 , respectively. This stress dependence of the surface energy arises primarily from two effects. First, while the difference between the stress levels within the wall and in the far field are essentially unchanged by the far field applied stress, the difference in the square of these stresses is affected, thereby changing the elastic contribution to the wall energy. The second factor arises due to the fact that ΔP_y across the wall increases with the applied stress due to the piezoelectric effect and this in turn increases the energy contribution due to $a_0 P_{y,x}^2$ within the domain wall.

Figs. 2a–c present the electromechanical fields near a stationary 90° domain wall for two different values of the parameter a_5 . In order to compute these results, the material properties are transformed such that the 1–2 material coordinates used to present the free energy in the Appendix are at 45° to the x and y -axes (see inset in Figs. 2a–c). The applied stress and applied electric field far from the domain are zero. Note that a larger value for a_5 increases the height of the barrier between spontaneous states rotated by 90°, and that a_5 has no effect on the 180° wall solutions.

The first observation from Figs. 2a–c is that for either value of a_5 the width of the domain wall is approximately $3l_0$ as opposed to $2l_0$ for the 180° wall. Also, the axial stress within the 90° wall is considerably lower than that within the 180° wall. One final comparison to the 180° wall can be made for the surface energy of the wall. Again using $a_0 = 1 \times 10^{-10} \text{ V m}^3/\text{C}$, and under no far field applied stress, for $a_5 = 0$ the surface energy is $\gamma_{90} = 4.81 \text{ mJ}/\text{m}^2$, and for $a_5 = 368 E_0/P_0^2$ is $\gamma_{90} = 6.29 \text{ mJ}/\text{m}^2$. Hence, the theory predicts that the 90° wall surface energy is on the order of one third of the 180° wall energy for barium titanate. This prediction is in qualitative accord with ab initio quantum mechanical computations on lead titanate that predict the 90° wall energy to be one fourth of the 180° wall energy (Meyer and Vanderbilt, 2002) (we have been unable to find similar simulation results for 90° walls in barium titanate). For the continuum theory, the disparity between the two 90° wall energies is due to the differences in the internal fields generated within the wall and the slight differences in the polarization gradients for the two values of a_5 .

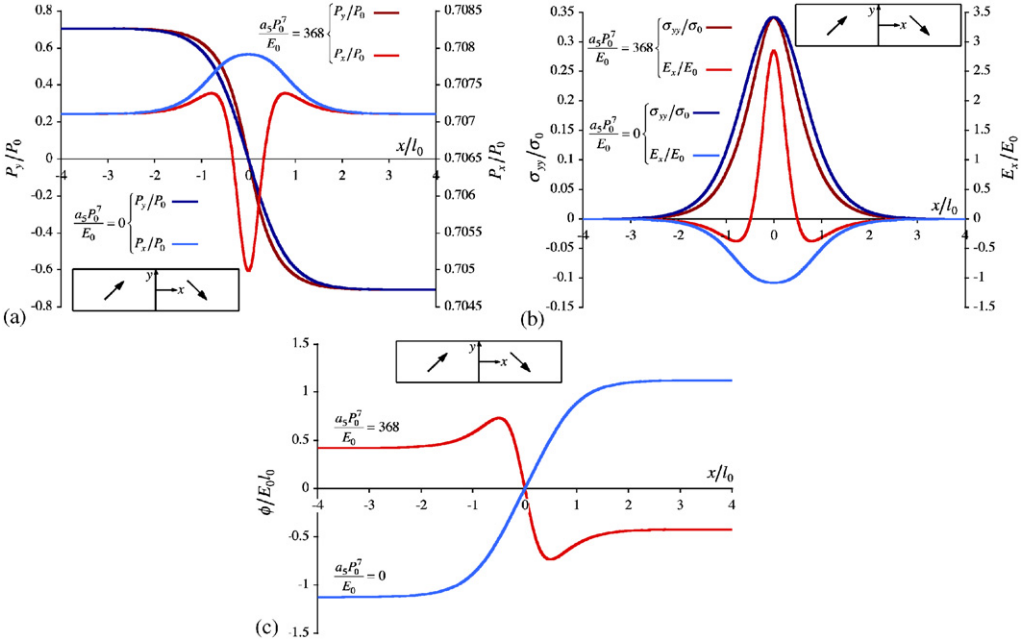


Fig. 2. (a) The polarization distributions near a stationary 90° domain wall for two different values of the parameter a_5 . The y -component of the polarization is given on the left ordinate axis and the x -component is given on the right ordinate axis. Note that the variations in P_x are relatively small, but result in large compensating levels of E_x (see Fig. 2b). (b) The stress and electric field distributions near a stationary 90° domain wall. The axial stress is given on the left ordinate axis and the x -component of the electric field is given on the right ordinate axis. (c) The electric potential distributions near a stationary 90° domain wall. Note that there is a jump in the electric potential across the domain wall and the sign of the jump and shape of the distribution are sensitive to the material parameter a_5 . The arrows in the small inset figures nominally represent the polarization on either side of the domain wall located at $x = 0$.

Considering the effects of the parameter a_5 , there is a qualitative difference in the behavior of P_x , increasing within the 90° wall for $a_5 = 0$ and decreasing within the wall for $a_5 = 368E_0/P_0^2$. Due to the constraint of charge compatibility, i.e. $D_x = 0$, this variation in P_x leads to a proportional variation in E_x , $E_x = -P_x/\kappa_0$, as shown in Fig. 2b. Qualitatively, one could imagine two extreme paths for the variations in the polarization near a 90° domain wall. The first type of path is akin to the magnetization within a magnetic domain wall where the magnitude of the polarization would remain constant but the direction would simply rotate through 90°. The second extremity would have the polarization trace the path in (P_x, P_y) from $(P_0/\sqrt{2}, P_0/\sqrt{2})$ to $(0, 0)$ to $(P_0/\sqrt{2}, -P_0/\sqrt{2})$. Both of these extreme paths are energetically unfavorable, and the actual path is very close to $(P_0/\sqrt{2}, P_0/\sqrt{2}) \rightarrow (P_0/\sqrt{2}, 0) \rightarrow (P_0/\sqrt{2}, -P_0/\sqrt{2})$, but low values of a_5 favor a slight distortion of this path towards the rotation of the polarization whereas higher values favor the slight distortion towards the reduction of the polarization.

The non-uniform levels of P_x and E_x within the domain wall necessarily require a variation in the electric potential near the domain wall, and in fact lead to a jump in the electric potential across the domain wall. For $a_5 = 368E_0/P_0^2$ this jump is $\Delta\phi/E_0 l_0 = -0.85$, and for $a_5 = 0$ the jump is $\Delta\phi/E_0 l_0 = 2.25$. This electric potential drop

has been predicted by ab initio computations on lead titanate, Meyer and Vanderbilt (2002), and has a significant effect on the interaction of domain walls with charge defects, Xiao et al. (2005). This feature of the domain wall solutions has interesting consequences for sharp interface model of domains which usually assume that the electric potential is continuous across a domain wall. These results suggest that the potential drop across the wall should be accounted for within the constitutive response of the wall in a fashion similar to that proposed by Gurtin et al. (1998) for mechanical interfaces.

The results to be presented in the following are for steadily propagating domain walls. Here the assumption will be made that the velocities are small with respect to the sound wave speeds in the material such that the inertial terms in Eqs. (3.4) and (3.5) can be neglected. In all cases the axial stress normal to the wall is $\sigma_{xx} = 0$, the out-of-plane strain is fixed at the spontaneous state $\varepsilon_{zz} = -0.329\varepsilon_0$ and the P_z , D_z , E_z , ε_{xz} , ε_{yz} , σ_{xz} , and σ_{yz} fields are zero. The 90° walls are subjected to simultaneous applied electric field E_y parallel to the domain wall and shear stress σ_{xy} with the average axial stress $\bar{\sigma}_{yy} = 0$ and $D_x = P_0/\sqrt{2}$. In the 90° wall case, either E_y or σ_{xy} is able to drive the motion of the domain wall in the absence of the other applied field. The 180° walls are subjected to simultaneous applied electric field E_y parallel to the domain wall and average axial stress $\bar{\sigma}_{yy}$. In this case the application of $\bar{\sigma}_{yy}$ in the absence of E_y does not cause domain wall motion, but $\bar{\sigma}_{yy}$ does alter the motion in the presence of E_y .

A discussion of the results of Fig. 3 are aided by linear piezoelectric approximations of the Eshelby driving traction and the jump in polarization across the domain wall. For the 90° wall with E_y and σ_{xy} applied, the linear piezoelectric approximation to the Eshelby driving traction and the polarization jumps across the domain wall are

$$f \approx \sqrt{2}P_0E_y + \underbrace{2.66\varepsilon_0}_{2\Delta\varepsilon_{xy}^0}\sigma_{xy}, \quad \Delta P_y \approx \sqrt{2}P_0 \text{ and } \Delta P_x = 0. \tag{3.12}$$

Then, for the 180° with E_y and $\bar{\sigma}_{yy}$ applied, the approximations are

$$f \approx 2\left(P_0 + \frac{d_{33}s_{11}^E - d_{31}s_{13}^E}{s_{11}^E}\bar{\sigma}_{yy}\right)E_y, \\ \Delta P_y \approx 2\left(P_0 + \frac{d_{33}s_{11}^E - d_{31}s_{13}^E}{s_{11}^E}\bar{\sigma}_{yy}\right) \text{ and } \Delta P_x = 0. \tag{3.13}$$

The first observation from Fig. 3 is that the mobility of 90° domain walls is greater than that of 180° walls. This can be predicted from Eq. (3.10) because the polarization gradients in a 180° wall are higher than those in the 90° walls. A rough calculation using Eq. (3.10) suggests that $\mu \propto t/\Delta P^2$ where t is the wall thickness. Then using Eqs. (3.12) and (3.13) and the approximation that the 90° wall thickness is about 1.5 times the thickness of a 180° wall yields $\mu_{90^\circ} \approx 3\mu_{180^\circ}$ when $\bar{\sigma}_{yy} = 0$. The *calculated* results at low driving traction levels place this ratio at 3 for $a_5 = 0$ and 2.3 for $a_5 = 368E_0/P_0^7$. The difference in the 90° wall mobility for materials corresponding to the two a_5 values can be explained from the slightly larger polarization gradients in the solution when $a_5 = 368E_0/P_0^7$ (see Fig. 2a).

A second observation from the 180° wall results is that the applied axial stress parallel to the domain wall has a noticeable effect on the wall mobility. This behavior is due to the fact that for an applied tensile stress the piezoelectric effect increases ΔP_y across the wall, which according to Eq. (3.10) decreases the mobility. Hence, the relationship between the driving traction f and the wall velocity v is not independent of the axial stress $\bar{\sigma}_{yy}$.

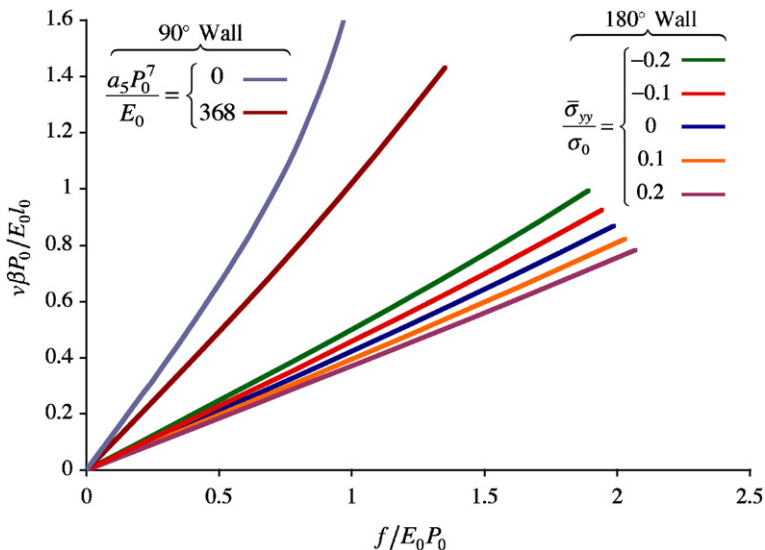


Fig. 3. Domain wall velocity versus the Eshelby driving traction for a 180° domain wall under different levels of applied stress, and for 90° domain walls in materials with different a_5 coefficients. For each level of the average applied stress $\bar{\sigma}_{yy}$, the driving force for the 180° wall is controlled solely by E_y ; however, each of the curves for the 90° walls contain data points from multiple combinations of applied electric field E_y and shear stress σ_{xy} .

Effectively, the domain wall mobility decreases as the average axial stress increases. We note that a similar behavior occurs for the 90° wall under an applied axial stress, but this effect has been omitted here for the sake of clarity on the plots in Fig. 3 and in this discussion. As for the electric potential drop, this feature of the solutions has interesting implications for sharp interface and other larger scale phenomenological constitutive theories for domain switching in ferroelectrics. Sharp interface theory Kessler and Balke (2001), single crystal continuum slip theory Huber et al. (1999), and polycrystalline flow theory Landis (2002b) have each identified the contribution to the driving force for switching associated with the changes in material properties due to switching. For the case of 180° switching these theories predict that a tensile stress will increase the driving force for switching when in combination with an electric field as in Eq. (3.13). However, these theories usually assume that the domain wall mobility or the critical switching strength is a constant value. In contrast, the phase-field theory predicts that the domain wall mobility is decreased by a tensile stress, and in fact this decrease in the mobility is greater, by a factor of 2 when linearized, than the increase in the driving force associated with the changes in the linear material properties, i.e. $f \sim 2EP_0(1 + d_{33}\bar{\sigma}_{yy}/P_0)$ but $\mu \sim 1/2\beta(P_0 + d_{33}\bar{\sigma}_{yy})^2 \approx (1 - 2d_{33}\bar{\sigma}_{yy}/P_0)/2\beta P_0^2$.

4. Finite element formulation

The governing equations for the phase-field model include Eqs. (2.1)–(2.9), (2.14), (2.15), and (2.18). When formulating a finite element method to solve these equations the field quantities that will be used as nodal degrees of freedom must first be identified. The simplest formulation, in terms of the smallest number of degrees of freedom per node,

would implement the components of mechanical displacement from which strain is derived, the components of electrical polarization from which the polarization gradient is derived, and the electrical potential or voltage from which electric field is derived. In order to implement such a formulation, the constitutive equations must take ε_{ij} , P_i , $P_{i,j}$, and E_i as the independent variables. However, the Helmholtz free energy has D_i instead of E_i as the independent variable. To address this difficulty, the following Legendre transformation is required to derive the electrical enthalpy h :

$$\begin{aligned}
 h(\varepsilon_{ij}, P_i, P_{i,j}, E_i) &= \psi - E_i D_i \\
 &= \frac{1}{2} a_{ijkl} P_{i,j} P_{k,l} + \frac{1}{2} \bar{a}_{ij} P_i P_j + \frac{1}{4} \bar{\bar{a}}_{ijkl} P_i P_j P_k P_l + \frac{1}{6} \bar{\bar{\bar{a}}}_{ijklm} P_i P_j P_k P_l P_m P_n \\
 &\quad + \frac{1}{6} \bar{\bar{\bar{a}}}_{ijklm} P_i P_j P_k P_l P_m P_n P_r P_s + b_{ijkl} \varepsilon_{ij} P_k P_l + \frac{1}{2} c_{ijkl} \varepsilon_{ij} \varepsilon_{kl} \\
 &\quad + f_{ijklm} \varepsilon_{ij} \varepsilon_{kl} P_m P_n + g_{ijklm} \varepsilon_{ij} P_k P_l P_m P_n - \frac{1}{2} \kappa_0 E_i E_i - E_i P_i, \quad (4.1)
 \end{aligned}$$

where the stresses, electric displacements, and micro-forces, ζ_{ij} and η_i , are derived as

$$\sigma_{ji} = \frac{\partial h}{\partial \varepsilon_{ij}}, \quad D_i = -\frac{\partial h}{\partial E_i}, \quad \zeta_{ji} = \frac{\partial h}{\partial P_{i,j}}, \quad \text{and} \quad \eta_i = \frac{\partial h}{\partial P_i}. \quad (4.2)$$

Then, given Eqs. (2.2), (2.4), (2.7), and (2.15), Eqs. (2.1), (2.3), (2.5), (2.6), and (2.9) can be derived from the following variational statement or principle of virtual work:

$$\begin{aligned}
 &\int_V \beta_{ij} \dot{P}_j \delta P_i \, dV + \int_V \rho \ddot{u}_i \delta u_i \, dV + \int_V \sigma_{ji} \delta \varepsilon_{ij} - D_i \delta E_i + \eta_i \delta P_i + \zeta_{ji} \delta P_{i,j} \, dV \\
 &= \int_V b_i \delta u_i - q \delta \phi + \gamma_i \delta P_i \, dV + \int_S t_i \delta u_i - \omega \delta \phi + \zeta_{ji} n_j \delta P_i \, dS. \quad (4.3)
 \end{aligned}$$

Eq. (4.3) is the foundation for the derivation of the finite element equations for the model. Again, the components of mechanical displacement, electric polarization, and the electric potential are used as nodal degrees of freedom. The strain, electric field and polarization gradient are derived within the elements, and finally the stress, electric displacement, and micro-forces are computed via Eqs. (4.1) and (4.2). We note that even though the polarization gradient appears in the free energy, C_0 continuous elements are in fact suitable for the solution. This is a fortuitous consequence of Eq. (2.8), given that both electric field and polarization can be taken as independent variables. Therefore, the polarization components take the same status as mechanical displacement and electric potential and the polarization gradient takes the same status as strain and electric field. If, for example, the electric field were the order parameter, and both electric potential and components of electric field were required as nodal degrees of freedom, then higher order elements would be required in the formulation.

Again, each node in the finite element mesh has mechanical displacement, polarization, and electric potential degrees of freedom. Then, defining the array of degrees of freedom as \mathbf{d} , each of the field quantities are interpolated from the nodal quantities with the same set of shape functions such that

$$\begin{Bmatrix} u_i \\ \phi \\ P_i \end{Bmatrix} = [\mathbf{N}]\{\mathbf{d}\}. \quad (4.4)$$

As mentioned previously, the shape function matrix \mathbf{N} must meet all of the requirements for standard C_0 continuous elements (Bathe, 1996). Hence, the displacements, electric potential, and polarization components are approximated by continuous functions throughout the mesh, but strains, electric fields, and polarization gradients will have jumps in certain components along element boundaries.

Ultimately the model can be used to predict microstructural evolution. Therefore, the governing equations must be integrated in time. Many problems of interest (in fact, all problems in the literature to date) are approximated in the mechanically quasi-static regime such that the inertia of the material is neglected, i.e. the second integral in Eq. (4.3) is ignored. The routines for such mechanically quasi-static cases are presented here. The discretized formulas for the polarization rates and the basic solution fields during a given time step are as follows,

$$\dot{P}_i = \frac{P_i^{t+\Delta t} - P_i^t}{\Delta t}, \quad (4.5)$$

$$u_i = \alpha u_i^{t+\Delta t} + (1 - \alpha)u_i^t, \quad \phi = \alpha \phi^{t+\Delta t} + (1 - \alpha)\phi^t \quad \text{and} \quad P_i = \alpha P_i^{t+\Delta t} + (1 - \alpha)P_i^t. \quad (4.6)$$

Here, the superscript indicates the time step at which the field is evaluated and α is a parameter between 0 and 1 that describes how the solution fields are interpolated in time during a given time step. When $\alpha = 0$ the first-order accurate forward Euler integration scheme is recovered, $\alpha = 1$ represents the first-order accurate backward Euler scheme that allows for enhanced numerical stability with larger time increments, and $\alpha = 0.5$ is the second-order accurate Crank–Nicholson method.

Given a known set of nodal degrees of freedom at time t , when the finite element interpolations of Eq. (4.4) and the time integration approximations of Eqs. (4.5) and (4.6) are substituted into Eq. (4.3), a set of non-linear algebraic equations results for the nodal degrees of freedom at $t + \Delta t$ that can be written in the form

$$\mathbf{B}(\mathbf{d}^{t+\Delta t}) = \mathbf{F}. \quad (4.7)$$

These equations are solved with the Newton–Raphson method:

$$\left. \frac{\partial \mathbf{B}}{\partial \mathbf{d}} \right|_{\mathbf{d}^{t+\Delta t}} \Delta \mathbf{d}_i = \mathbf{F} - \mathbf{B}(\mathbf{d}_i^{t+\Delta t}), \quad (4.8)$$

where i is the current step counter in the Newton–Raphson sequence and $\Delta \mathbf{d}_i$ is the increment computed for $\mathbf{d}_i^{t+\Delta t}$ such that $\mathbf{d}_i^{t+\Delta t} = \mathbf{d}_{i-1}^{t+\Delta t} + \Delta \mathbf{d}_i$. Note that the first term of Eq. (4.8) is the Newton–Raphson Jacobian matrix, and for the formulation associated with Eq. (4.3) this matrix is symmetric and banded. The Newton–Raphson procedure is carried out until a suitable level of convergence is obtained yielding a solution for the displacement, electric potential, and polarization fields at time step $t + \Delta t$. With this new set of known nodal degrees of freedom in hand, the next time increment is computed by solving the updated form of Eq. (4.7), and the procedure continues to march through time.

5. Domain wall interactions with line charge defects

In this section the finite element formulation is applied to investigate the interactions of domain walls with regular arrays of line charge defects. The configurations for the array of charges for the 180° and 90° walls are shown in Figs. 4a–d.

As in Section 3 the nominal normal direction to the domain wall will be in the x -direction. The charged lines are extended in the z -direction and separated by a distance h along the y -direction. All calculations are for equilibrium domain structures and so the inverse mobility tensor β is irrelevant and can be taken to be zero. The other material parameters are characteristic of barium titanate at room temperature and are listed in the Appendix. The parameter $a_5 = 368E_0/P_0^7$ for each of these simulations. Due to the periodicity of the charge array, only a strip of material with a single centered charge needs to be analyzed. The length of the strip along the x -direction is $\sim 100\text{--}300l_0$ depending on the array spacing h , and was chosen such that the effects associated with the edges were not apparent. Periodic boundary conditions are applied along the top (+) and bottom (–) surfaces of the strip such that $P_x^+(x) = P_x^-(x)$, $P_y^+(x) = P_y^-(x)$, $u_x^+(x) = u_x^-(x) + h\partial u_x/\partial y$, $u_y^+(x) = u_y^-(x) + \varepsilon_{yy}h$, and $\phi^+(x) = \phi^-(x) - E_y h$, where $\partial u_x/\partial y$, ε_{yy} , and E_y are the applied simple shear strain, axial strain, and electric field, respectively. Note that the simple shear strain and axial strain represent changes from the unloaded spontaneous state. The left and right boundaries of the rectangular region are kept at zero traction, zero micro-force η_x and η_y , and surface charge density consistent with the x -component of the spontaneous polarization and the net charge of the line charge array.

The first set of results to be presented are for the interaction of a 180° domain wall with an array of line charges each with a charge per unit length of Q and separated by a vertical distance h . Both the applied simple shear and the axial strain are taken to be zero for these simulations. Figs. 5a–c illustrate the evolution of the equilibrium domain structure as the applied electric field is increased, with (a) at zero applied field and (c) at a level of applied field just before that where the domain wall breaks through the charge array. The first observation from these simulations is that the charge array creates kinks in the domain wall. These kinks are the significant features that cause the interaction of the 180° wall with the charges. Also of note is the fact that even just before the wall breaking through the defects there is very little bowing of the wall, approximately half the domain wall thickness just before the breaking field for this array. However, even this seemingly small level of bowing results in a significant “anelastic” or extrinsic contribution to the dielectric properties of a multi-domain material. For example, at a domain wall density of

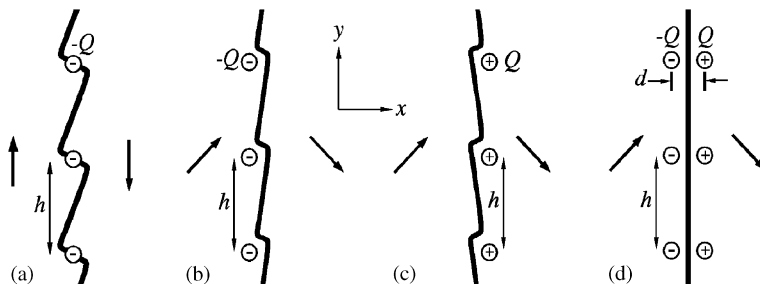


Fig. 4. The configurations investigated for the interactions of domain walls with arrays point charge defects are illustrated above. (a) A 180° wall with an array of negative point charges. The interaction of a 180° wall with an array of positive point charges is mirror symmetric to the negative charge array. (b) A 90° wall with an array of negative point charges. (c) A 90° wall with an array of positive point charges. (d) A 90° wall with an array of point charge dipoles. Results for the critical electric field and stress combinations for the wall to break through the array are presented in later figures.

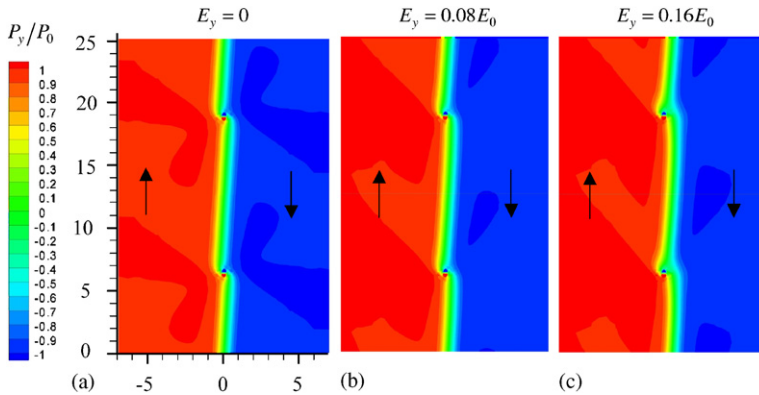


Fig. 5. The P_y/P_0 polarization distribution near a 180° domain wall interacting with an array of line charges. The lines are negatively charged at a level of $Q = 1.26P_0l_0$, separated by a distance $h = 12.6l_0$, and can be seen as the small red and blue circles. Red indicates polarization in the positive y -direction and blue in the negative y -direction. The x and y scales are normalized by l_0 . Periodic boundary conditions are enforced on the lines at half of the distance between the charges. Electric field is applied in the y -direction until the domain wall is able to break through the charge array. Figures a–c depict the equilibrium domain wall configuration for applied field levels of (a) $E_y = 0$, (b) $E_y = 0.08E_0$ and (c) $E_y = 0.16E_0$. The field level in (c) is very close to the breaking strength for this particular charge array.

$\rho_{\text{wall}} = 10^7 \text{ m}^2/\text{m}^3$ (corresponding to domain thicknesses of 100 nm) and a coercive field of $E_c = 3.5 \text{ MV}/\text{m}^2$ (characteristic of the strength of the array in Fig. 5c), the intrinsic contribution to the electric displacement is $\kappa_{33}E_c \sim 5 \times 10^{-3} \text{ C}/\text{m}^2$ and the extrinsic contribution is $2P_0\rho_{\text{wall}}\delta \sim 5 \times 10^{-3} \text{ C}/\text{m}^2$ where δ is the deflection of the domain wall. Hence even for this small level of bowing on the order of 1 nm, the extrinsic contribution to the dielectric properties is of the same order of magnitude as the intrinsic contribution.

The interaction between the charges and the 180° domain wall illustrated in Fig. 5 is contrary to another recent investigation on charge–domain wall interactions by Xiao et al. (2005). Xiao et al. (2005) treat charge defects as a continuum distribution and allow for the diffusion of the charge density due to gradients in the concentration of charge and interactions with the local electric field. Within a phase-field framework Xiao et al. (2005) find that the charge distribution does not interact (or interacts very weakly) with 180° domain walls but creates a dipole layer around 90° domain walls. These results are consistent with those of Fig. 2. Specifically, no electric field is created by a straight 180° domain wall and hence the wall does not cause a force on the charge distribution, whereas charges will interact with the 90° domain wall by setting up a dipole layer to decrease component of electric field normal to wall.

The fundamental difference between the model of Xiao et al. (2005) and the results of Fig. 5 lies in the continuum versus discrete description of the charges. If there is no variation of the continuum charge distribution along the y -direction then the domain wall will remain straight, and straight 180° domain walls do not induce electric fields that can interact with the charge distribution. However, discrete charges cause electric field distributions in the material that tend to kink 180° domain walls as shown in Fig. 5a. In contrast to a straight wall, the kinked wall will cause electric fields due to the requirements of charge “compatibility,” and these electric fields will in turn interact with the charge defects. A second physical effect that will cause charges to interact with domain walls is if

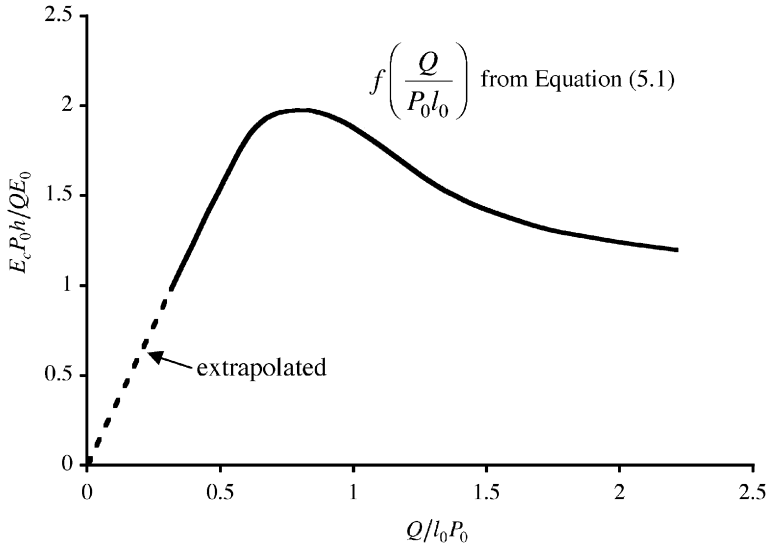


Fig. 6. The critical electric field E_c required for a 180° domain wall to break through an array of charge defects of the configuration illustrated in Fig. 4a has a $1/h$ dependence as given in Eq. (5.1). The dimensionless function f is of order unity and is plotted here.

the charges are due to oxygen vacancies. In this case, the dilatant strain field of the vacancy will interact with the high tensile stresses within the 180° domain wall. This effect has not been included in either this model or that of Xiao et al. (2005).

Within the phase-field theory, if the inverse mobility β is assumed to be a constant then domain walls will move at infinitesimally small applied electric fields in a defect free material. However, as illustrated in Fig. 5, an array of defects acts to pin the domain walls such that significant domain wall motion cannot occur unless the applied electric field reaches a critical level. Using this model, the existence of a finite coercive field can be explained from the interaction of defects with the domain walls. Furthermore, the spacing of the defects has a significant effect on the coercive field with smaller spacing leading to larger coercive fields. Specifically, within the range of defect charges, $0.25P_0l_0 < Q < 2.5P_0l_0$, and spacings, $1.6l_0 < h < 12.6l_0$, that we have investigated, the results for the critical breaking field, E_c , show a $1/h$ dependence such that

$$\frac{E_c}{E_0} = f\left(\frac{Q}{P_0l_0}\right) \frac{Q}{P_0h}. \tag{5.1}$$

The function f is of order unity for the range of $0.25 < Q/P_0l_0 < 2.5$ and is plotted in Fig. 6. Note that the results suggest that $f \rightarrow 0$ as $Q/P_0l_0 \rightarrow 0$. Such behavior, and in general the fact that f is not a constant, is a result of the finite domain wall thickness and the interaction of the length scales Q/P_0 and l_0 , and cannot be predicted from a sharp interface description of domain walls.

We have also investigated the effects of an applied axial stress along the y -direction on the critical electric field required for the wall to pass through the array. Recall that the Eshelby driving traction on the wall increases with increasing tensile stress and decreases for an applied compressive stress due to the effects of the change in piezoelectric properties

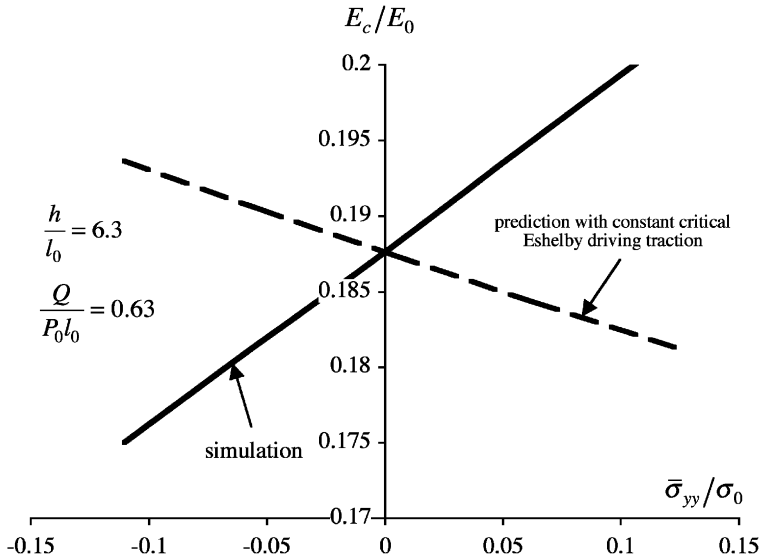


Fig. 7. The effects of an applied axial stress parallel to the domain wall on the critical electric field required for a 180° domain wall to break through the charge array.

across the domain wall. However, for moving domain walls, this increase in driving traction is offset by a larger decrease in mobility, causing such walls to travel more slowly under a tensile stress than a compressive stress. The present simulations compute equilibrium configurations and hence the kinetic effects associated with the mobility are not a factor. Therefore, if one were to only consider the effects of the axial stress on the Eshelby driving traction, then it would be expected that the critical electric field to break through the array should decrease when in combination with a tensile stress and increase for applied compressive stresses. Such behavior is illustrated in Fig. 7 as the dashed line. The critical driving traction for this curve has been fit to the $\bar{\sigma}_{yy} = 0$ simulation point. Contrary to this prediction, the simulation results presented in Fig. 7 indicate that the critical electric field required for the wall to pass through the charge array *increases* as the applied average axial stress increases. Again, this behavior cannot be explained by the assumed kinetic relationships within the phase-field model, since kinetics plays no role in these equilibrium simulations. Instead, this behavior is due to the complexities of the energetic interactions between the domain wall and the charge defects. As for the moving wall cases, these results suggest that phenomenological theories which assume domain switching occurs when an Eshelby-like driving force reaches a constant critical value will incorrectly predict the effects of the energetic terms associated with the changes in the piezoelectric properties.

The final sets of results to be presented are for the interactions of a 90° domain wall with arrays of charge dipoles. Unlike the 180° wall, which has an equilibrium position centered on the charge array, the equilibrium position of the 90° wall is offset from the array due to the x -component of electric field within the wall. Figs. 4b and c are schematics of the zero load equilibrium configurations of a 90° wall with negative and positive charge arrays. The configuration illustrated in Fig. 4d is motivated by the work of Xiao et al. (2005) who

predicted that the interactions of a mobile charge density with domain walls will cause evolution towards a charge dipole layer near 90° domain walls. The applied loadings to the system include an electric field parallel to the domain wall $E_y = E$ and a simple shear strain $\partial u_x / \partial y$ applied in order to create a shear stress $\sigma_{xy} = \tau$. In all cases the far field axial stress $\bar{\sigma}_{xx} = 0$, the far field changes in the axial strains from the initial remanent state are zero, $\Delta \bar{\epsilon}_{yy} = 0$ and $\Delta \bar{\epsilon}_{zz} = 0$, and the far field electric displacement in the direction normal to the domain wall is $\bar{D}_x = \sqrt{2}P_0$.

Figs. 8a–c illustrate the equilibrium configurations of a 90° domain wall with an array of charges with $Q = 0.32P_0l_0$ and $h = 6.3l_0$ for (a) the configuration from Fig. 4d with $d = 1.6l_0$ and zero applied loading, (b) the configuration from Fig. 4c with zero applied loading, and (c) the configuration from Fig. 4c with applied shear stress just before the critical breaking stress, i.e. $E = 0$ and $\tau = 0.159\sigma_0$. Of note, and not depicted in Fig. 8, is the fact that just before breaking through the dipole array, the domain wall configuration is similar for either the purely electrical loading or the purely mechanical loading. Furthermore, the configuration of the domain wall shown in Fig. 8a just before breaking through the array is quite similar to that shown in Fig. 8c but occurs at a lower level of combined electromechanical loading than the configuration of Fig. 8c. As for the 180° domain wall, the small motion of the 90° wall prior to breaking through the array leads to significant anelastic or extrinsic contributions to the linear properties of the material. However, for the case of the 90° wall the dielectric permittivity, elastic compliance, and piezoelectric properties are all enhanced, while for the 180° wall only the dielectric permittivity is increased significantly.

Fig. 9 plots “switching surfaces” in $E-\tau$ space for the three 90° domain wall configurations depicted in Fig. 4. To within the accuracy of the simulations the critical combinations of normalized electric field and shear stress fall on the same line for each of the three possible 90° domain wall types. The only parameter that differentiates the

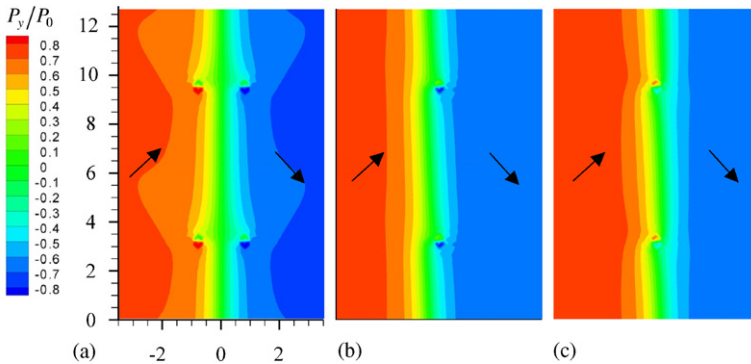


Fig. 8. The P_y/P_0 polarization distribution near a 90° domain wall interacting with an array of line charges, $Q = 0.32P_0l_0$ and $h = 6.3l_0$. Red indicates polarization in the positive y -direction and blue in the negative y -direction. The x and y scales are normalized by l_0 . Periodic boundary conditions are enforced on the lines at half of the distance between the charges. Electric field and shear stress are applied until the domain wall is able to break through the charge array. Figures a–c depict the equilibrium domain wall configuration for applied field levels of (a) $d = 1.6l_0$, $E = 0$ and $\tau = 0$ for the configuration from Fig. 4a, (b) $E = 0$ and $\tau = 0$ for the configuration from Fig. 4c, and (c) $E = 0$ and $\tau = 0.159\sigma_0$ for the configuration from Fig. 4c. The load level in (c) is very close to the breaking strength for this particular charge array.

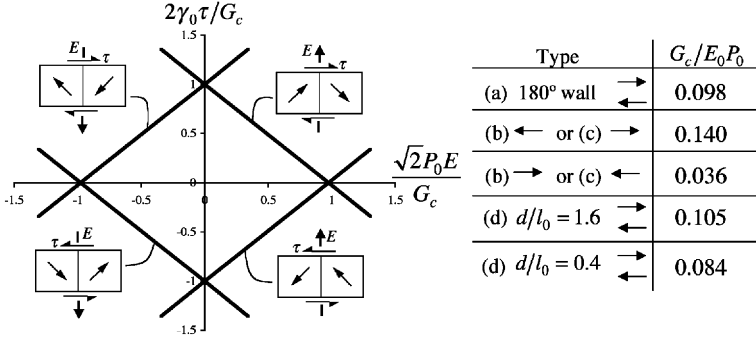


Fig. 9. The “switching surface” for each of the three 90° domain wall types and motion directions. The line charges have magnitude $Q = 0.32P_0l_0$ and are separated by $h = 6.3l_0$. The linear relationships between the critical combinations of shear stress and the electric field have not been assumed but rather verified by the simulations. The table lists the critical energy density G_c required to break through the array for each of the domain wall/charge array interactions depicted in Fig. 4.

different array types is the critical energy G_c required to break through the array. Each combination of array configuration and domain wall motion direction corresponds to a rhombus of different size, associated with the specific G_c , but identical shape. The critical energies are given in the table in Fig. 9 for each of the array types (a)–(d), corresponding to the schematics in Figs. 4a–d, and domain wall motion directions, \rightarrow or \leftarrow . For load states inside the rhombus formed by the four lines, the domain wall will return to its equilibrium position when the applied stress and electric field are removed from the system. When the load state reaches one of the lines, i.e. $\sqrt{2}P_0E + 2\gamma_0\tau = G_c$, that specific 90° domain wall type will break through the charge array resulting in significant domain switching. For the 180° domain wall the breaking criterion is $2P_0E = G_c$.

The fact that the switching surface is described by lines of the form $\sqrt{2}P_0E + 2\gamma_0\tau = G_c$ for 90° domain wall motion and $2P_0E = G_c$ for 180° domain wall motion implies that there exists an approximate normality relationship between the switching surface and the increments of remanent strain and polarization in the crystal. We have included the caveat of “approximate normality” due to the previous results shown in Fig. 7, illustrating the dependence of G_c on the axial stress parallel to the domain wall. It may be possible (and valuable) to construct a rigorous normality framework, but such a theory will differ from that already established in other phenomenological theories (Kessler and Balke, 2001; Huber et al., 1999; Landis 2002a, b).

6. Discussion

In this work a new approach for the derivation of the time-dependent Ginzburg–Landau equation i.e. Eq. (2.16), governing the evolution of the polarization order parameter in a ferroelectric crystal has been presented. The key idea is that generalized micro-forces are postulated that do work as the order parameter changes. An overall balance of these micro-forces is then established taking the same physical footing as mechanical equilibrium and Gauss’ law, i.e. this balance law must hold for all materials. It was then shown, by applying established continuum methods for analyzing the consequences of the second law of thermodynamics, that the micro-force balance ultimately leads to the commonly

accepted Ginzburg–Landau evolution equations for the order parameter. The following question can then be posed, have we gained anything by introducing such micro-forces? We would argue that in fact we have. All of reversible, small-deformation, static, mechanics can be established by postulating a strain energy density $\psi(\varepsilon_{ij})$ and minimizing the potential energy of the system subject to the constraints of linear kinematics, i.e. $\varepsilon_{ij} = (u_{i,j} + u_{j,i})/2$. Such a procedure leads to the following set of partial differential equations and boundary conditions,

$$\left(\frac{\partial\psi}{\partial\varepsilon_{ij}}\right)_j + b_i = 0 \text{ in } V \text{ and } \frac{\partial\psi}{\partial\varepsilon_{ij}}n_j = t_i \text{ on } S. \quad (6.1)$$

However, Eq. (6.1) is simply a combination of mechanical equilibrium and the constitutive law $\sigma_{ji} = \partial\psi/\partial\varepsilon_{ij}$. Hence, by minimizing the potential energy of the system, the physical content of the stresses and their balance (mechanical equilibrium) is obscured. Therefore, we take the view that within the phase-field setting Eq. (2.9) has the same fundamental physical priority as Eqs. (2.1)–(2.8). A second rationale for postulating the micro-forces is that in the presence of other dissipative mechanisms like conductive heat transfer or the diffusion of species within the material, the micro-force balance can be applied within the second law of thermodynamics using the systematic approach established by Coleman and Noll (1963) to determine the constraints on the constitutive dependencies.

Within the phase-field framework it is appropriate to consider the domain walls as a set of internal boundary layers that move through the material. The domain wall thickness length scale associated with these “boundary layers” is $l_0 = \sqrt{a_0 P_0/E_0}$. Unlike sharp interface theories that require a specification of the surface energy of the interfaces, the phase-field theory *predicts* the energy content of the different domain wall types. This surface energy is dependent both on the exchange energy parameter a_0 , and on the features of the free energy landscape. For a given free energy functional, the domain wall surface energies are proportional to $\sqrt{a_0}$. Note that simulation results generated by manipulating (i.e. increasing) a_0 for the purpose of computational convenience must be interpreted carefully since such a procedure changes the surface energy of the domain walls. When simulating the qualitative response of ferroelectric crystals, increasing a_0 for computational expediency is likely to yield reasonable behavior. However, for quantitative predictions of domain structures and the interactions of domain walls with defects, a more accurate representation of the surface energy is required. Given the disparate length scales associated with the domain wall thickness $\sim l_0$ and the domain structure size $\sim 100\text{--}1000l_0$, accurate numerical solutions to large-scale domain structure evolution problems will require computational schemes that allow for adaptive mesh refinement (Provatas et al., 1998).

As for the derivation of the governing equations, the finite element formulation presented here is also a departure from several of the prior studies on phase-field modeling of ferroelectrics that have applied spectral methods for the numerical solutions. One benefit of the finite element formulation is the ability to apply any arbitrary form for the material free energy that includes the general anisotropy for elastic and piezoelectric properties. The finite element method also allows for the analysis of arbitrary geometries with very general non-periodic or periodic boundary conditions. Examples where such flexibility is useful include the analysis of domain wall interactions with point or line defects, like those presented in Section 5, or investigations of domain switching and

nucleation near crack tips by applying asymptotic crack tip boundary conditions in the far field and the appropriate electromechanical boundary conditions on the crack faces (Landis, 2004). Finally, when solutions for the electric fields in all of free space are required, e.g. domain patterns near free surfaces, then more sophisticated boundary conditions like the Dirichlet to Neumann (DtN) map can be added to the finite element method (Givoli and Keller, 1989) to solve such problems.

The methods presented here, including both the introduction of micro-forces and their balance, and the finite element formulation, can be generalized for the analysis of a wide range of ferroic materials, including shape memory alloys, ferromagnetic materials, magneto-electric materials (BiFeO₃), and ferromagnetic shape memory alloys. Of course, in these cases the order parameter is not necessarily the material polarization and the details of the physical behavior will also differ. For example, in ferromagnetic materials the order parameter will be the magnetization, and, in contrast to electrical polarization, the magnetization will rotate its direction without reducing in magnitude. These differences characterize the specific details of the physical behavior, but the concepts associated with the diffuse interface description of domain walls, micro-forces and their balance, and the numerical techniques can be applied universally to this broad class of materials.

Acknowledgments

The authors would like to acknowledge support from the Office of Naval Research Grant no. N00014-03-1-0537. Special thanks to Johannes Rödel for pointing out the effect of small levels of domain wall bowing on the extrinsic dielectric, elastic and piezoelectric properties.

Appendix

The general form for the Helmholtz free energy applied in this work is given in Eq. (2.18). In a coordinate system with the Cartesian axes aligned with the $\langle 100 \rangle$ directions, a form of the free energy that can be used to mimic the properties of single crystals that undergo a cubic to tetragonal phase transformation through the Curie temperature is

$$\begin{aligned} \psi = & \frac{a_0}{2} \left(P_{1,1}^2 + P_{2,2}^2 + P_{3,3}^2 + P_{1,2}^2 + P_{2,1}^2 + P_{1,3}^2 + P_{3,1}^2 + P_{2,3}^2 + P_{3,2}^2 \right) \\ & + \frac{a_1}{2} (P_1^2 + P_2^2 + P_3^2) + \frac{a_2}{4} (P_1^4 + P_2^4 + P_3^4) + \frac{a_3}{2} (P_1^2 P_2^2 + P_2^2 P_3^2 + P_1^2 P_3^2) \\ & + \frac{a_4}{6} (P_1^6 + P_2^6 + P_3^6) + a_6 (P_1^4 (P_2^2 + P_3^2) + P_2^4 (P_1^2 + P_3^2) + P_3^4 (P_1^2 + P_2^2)) \\ & + \frac{a_5}{4} (P_1^4 P_2^4 + P_2^4 P_3^4 + P_1^4 P_3^4) - \frac{b}{2_1} (\varepsilon_{11} P_1^2 + \varepsilon_{22} P_2^2 + \varepsilon_{33} P_3^2) \\ & - \frac{b_2}{2} ((\varepsilon_{22} + \varepsilon_{33}) P_1^2 + (\varepsilon_{11} + \varepsilon_{33}) P_2^2 + (\varepsilon_{11} + \varepsilon_{22}) P_3^2) b_3 ((\varepsilon_{12} + \varepsilon_{21}) P_1 P_2 \\ & + (\varepsilon_{13} + \varepsilon_{31}) P_1 P_3 + (\varepsilon_{23} + \varepsilon_{32}) P_2 P_3) + \frac{c_1}{2} (\varepsilon_{11}^2 + \varepsilon_{22}^2 + \varepsilon_{33}^2) \\ & + c_2 (\varepsilon_{11} \varepsilon_{22} + \varepsilon_{11} \varepsilon_{33} + \varepsilon_{22} \varepsilon_{33}) + \frac{c_3}{2} (\varepsilon_{12}^2 + \varepsilon_{21}^2 + \varepsilon_{13}^2 + \varepsilon_{31}^2 + \varepsilon_{23}^2 + \varepsilon_{32}^2) \\ & + \left(\frac{f_1}{2} \varepsilon_{11}^2 + \frac{f_2}{2} (\varepsilon_{22}^2 + \varepsilon_{33}^2) + f_3 (\varepsilon_{11} \varepsilon_{22} + \varepsilon_{11} \varepsilon_{33}) + f_4 \varepsilon_{22} \varepsilon_{33} + \frac{f_5}{2} (\varepsilon_{12}^2 + \varepsilon_{21}^2 + \varepsilon_{13}^2 + \varepsilon_{31}^2) \right) \end{aligned}$$

$$\begin{aligned}
 & + \frac{f_6}{2}(\varepsilon_{23}^2 + \varepsilon_{32}^2) \Big) P_1^2 + \left(\frac{f_1}{2} \varepsilon_{22}^2 + \frac{f_2}{2}(\varepsilon_{11}^2 + \varepsilon_{33}^2) + f_3(\varepsilon_{11}\varepsilon_{22} + \varepsilon_{22}\varepsilon_{33}) \right. \\
 & + f_4\varepsilon_{11}\varepsilon_{33} + \frac{f_5}{2}(\varepsilon_{12}^2 + \varepsilon_{21}^2 + \varepsilon_{23}^2 + \varepsilon_{32}^2) + \frac{f_6}{2}(\varepsilon_{13}^2 + \varepsilon_{31}^2) \Big) P_2^2 \\
 & + \left(\frac{f_1}{2} \varepsilon_{33}^2 + \frac{f_2}{2}(\varepsilon_{11}^2 + \varepsilon_{22}^2) + f_3(\varepsilon_{11}\varepsilon_{33} + \varepsilon_{22}\varepsilon_{33}) + f_4\varepsilon_{11}\varepsilon_{22} \right. \\
 & + \frac{f_5}{2}(\varepsilon_{13}^2 + \varepsilon_{31}^2 + \varepsilon_{23}^2 + \varepsilon_{32}^2) + \frac{f_6}{2}(\varepsilon_{12}^2 + \varepsilon_{21}^2) \Big) P_3^2 \\
 & + \left(\frac{g_1}{4} \varepsilon_{11} + \frac{g_2}{4}(\varepsilon_{22} + \varepsilon_{33}) \right) P_1^4 + \left(\frac{g_1}{4} \varepsilon_{22} + \frac{g_2}{4}(\varepsilon_{11} + \varepsilon_{33}) \right) P_2^4 \\
 & + \left(\frac{g_1}{4} \varepsilon_{33} + \frac{g_2}{4}(\varepsilon_{11} + \varepsilon_{22}) \right) P_3^4 + \frac{g_3}{4}(\varepsilon_{12} + \varepsilon_{21})(P_1P_2^3 + P_2P_1^3) \\
 & + \frac{g_3}{4}(\varepsilon_{13} + \varepsilon_{31})(P_1P_3^3 + P_3P_1^3) + \frac{g_3}{4}(\varepsilon_{23} + \varepsilon_{32})(P_2P_3^3 + P_3P_2^3) \\
 & + \frac{1}{2\kappa_0} ((D_1 - P_1)^2 + (D_2 - P_2)^2 + (D_3 - P_3)^2).
 \end{aligned}$$

The properties of mono-domain single crystal barium titanate have been measured by Li et al. (1991) at room temperature ($\sim 22^\circ\text{C}$). For a domain with spontaneous polarization in the x_3 direction, the spontaneous polarization and strain state is

$$\begin{aligned}
 P_3^s &= 0.26 \text{ C/m}^2, \quad P_1^s = P_2^s = 0, \quad \varepsilon_{33}^s = 0.0082, \\
 \varepsilon_{11}^s &= \varepsilon_{22}^s = -0.0027, \quad \varepsilon_{12}^s = \varepsilon_{13}^s = \varepsilon_{23}^s = 0.
 \end{aligned}$$

In the same coordinate system, the elastic, piezoelectric, and dielectric properties given in standard Voight notation are:

$$\begin{aligned}
 s_{11}^E &= 8.01 \times 10^{-12} \text{ m}^2/\text{N}, \quad s_{12}^E = -1.57 \times 10^{-12} \text{ m}^2/\text{N}, \quad s_{13}^E = -4.6 \times 10^{-12} \text{ m}^2/\text{N}, \\
 s_{33}^E &= 12.8 \times 10^{-12} \text{ m}^2/\text{N}, \quad s_{44}^E = 17.8 \times 10^{-12} \text{ m}^2/\text{N}, \quad s_{66}^E = 7.91 \times 10^{-12} \text{ m}^2/\text{N}, \\
 d_{33} &= 106 \times 10^{-12} \text{ C/N}, \quad d_{31} = -50 \times 10^{-12} \text{ C/N}, \quad d_{15} = 580 \times 10^{-12} \text{ C/N}, \\
 \kappa_{11}^\sigma &= 4100\kappa_0 = 36.3 \times 10^{-9} \text{ F/m}, \quad \kappa_{33}^\sigma = 160\kappa_0 = 1.42 \times 10^{-9} \text{ F/m}, \\
 \kappa_0 &= 8.854 \times 10^{-12} \text{ F/m} \quad (\text{dielectric permittivity of free space}).
 \end{aligned}$$

Note that Li et al. (1991) report the dielectric permittivities at constant strain $\kappa_{11}^\varepsilon = 1980\kappa_0$ and $\kappa_{33}^\varepsilon = 48\kappa_0$. Therefore, the permittivities at constant stress presented above are calculated accordingly. Then, in order to fit these properties of a mono-domain the coefficients of the Helmholtz free energy are chosen as follows:

$$\begin{aligned}
 a_1 &= -0.668325E_0/P_0, & a_2 &= -3.80653E_0/P_0^3, & a_3 &= 0.78922E_0/P_0^3, \\
 a_4 &= 12.4421E_0/P_0^5, & a_6 &= 0.134226E_0/P_0^5, \\
 b_1 &= 2.54138E_0/\varepsilon_0P_0, & b_2 &= 1.74267E_0/\varepsilon_0P_0, & b_3 &= 0.399353E_0/\varepsilon_0P_0, \\
 c_1 &= 2.04999\sigma_0/\varepsilon_0, & c_2 &= 0.971673\sigma_0/\varepsilon_0, & c_3 &= 1.27976\sigma_0/\varepsilon_0, \\
 f_1 &= 0.663581E_0/\varepsilon_0^2P_0, & f_2 &= 0.841326E_0/\varepsilon_0^2P_0, & f_3 &= -0.170635E_0/\varepsilon_0^2P_0, \\
 f_4 &= 0.687281E_0/\varepsilon_0^2P_0, & f_5 &= 0.106647E_0/\varepsilon_0^2P_0, & f_6 &= 0.213294E_0/\varepsilon_0^2P_0, \\
 g_1 &= -3.66149E_0/\varepsilon_0^2P_0^3, & g_2 &= 6.27423E_0/\varepsilon_0^2P_0^3, & g_3 &= -1.21644E_0/\varepsilon_0^2P_0^3,
 \end{aligned}$$

where $P_0 = 0.26 \text{ C/m}^2$, $\varepsilon_0 = 0.0082$, $E_0 = 2.18247 \times 10^7 \text{ V/m}$, and $\sigma_0 = E_0 P_0 / \varepsilon_0 = 692 \times 10^6 \text{ N/m}^2$. The definitions of P_0 and ε_0 obviously arise from the spontaneous state. The critical electric field E_0 is the magnitude of the electric field required to cause homogeneous 180° switching when the electric field is applied in the opposite direction of the uniform spontaneous polarization. Finally, the stress σ_0 is simply a derived quantity used for normalizations.

The tetragonal elastic properties alone do not uniquely determine the c and f coefficients. Hence, the c 's have been fit to the cubic elastic properties of the paraelectric phase of barium titanate as measured at 150°C by Berlincourt and Jaffe (1958). We have also selected values for a_1 and a_3 to be in agreement to those reported by Pertsev et al. (1998) as these parameters primarily affect the characteristics of the energy wells.

Note that the coefficients a_0 and a_5 do not affect the fitting of the coefficients to the measured material properties. The parameter a_5 has been discussed in detail by Zhang and Bhattacharya (2005a), and it primarily affects the energy barrier along a line connecting adjacent energy wells in polarization space. In this work a_5 has been chosen to be either zero or $368E_0/P_0^7$. The coefficient a_0 is important in determining the domain wall thickness and domain wall surface energy. For $a_0 = 1 \times 10^{-10} \text{ V m}^3/\text{C}$ the theory predicts 180° domain walls on the order of 2 nm thick with a surface energy of approximately 15 mJ/m^2 .

References

- Ahluwalia, R., Cao, W., 2000. Influence of dipolar defects on switching behavior in ferroelectrics. *Phys. Rev. B* 63, 012103–012114.
- Ahluwalia, R., Cao, W., 2001. Size dependence of domain patterns in a constrained ferroelectric system. *J. Appl. Phys.* 89, 8105–8109.
- Allik, H., Hughes, T.J.R., 1970. Finite element method for piezoelectric vibration. *Int. J. Numer. Methods Eng.* 2, 151–157.
- Bathe, K.J., 1996. *Finite Element Procedures*. Prentice-Hall, New Jersey.
- Berlincourt, D., Jaffe, H., 1958. Elastic and piezoelectric coefficients of single-crystal barium titanate. *Phys. Rev.* 111, 143–148.
- Cao, W., Cross, L.E., 1991. Theory of tetragonal twin structures in ferroelectric perovskites with a first-order phase transition. *Phys. Rev. B* 44, 5–12.
- Cohen, R.E., Krakauer, H., 1992. Electronic structure studies of differences in ferroelectric behavior of BaTiO_3 and PbTiO_3 . *Ferroelectrics* 136, 65–83.
- Coleman, R.D., Noll, W., 1963. The thermodynamics of elastic materials with heat conduction and viscosity. *Arch. Rational Mech. Anal.* 13, 167–178.
- Devonshire, A.F., 1954. Theory of ferroelectrics. *Philos. Mag. Suppl.* 3, 85.
- Fried, E., Gurtin, M.E., 1993. Continuum theory of thermally induced phase transitions based on an order parameter. *Physica D* 68, 326–343.
- Fried, E., Gurtin, M.E., 1994. Dynamic solid–solid transitions with phase characterized by an order parameter. *Physica D* 72, 287–308.
- Givoli, D., Keller, J.B., 1989. A finite-element method for large domains. *Comp. Methods Appl. Mech. Eng.* 76, 41–66.
- Gurtin, M.E., 1996. Generalized Ginzburg–Landau and Cahn–Hilliard equations based on a microforce balance. *Physica D* 92, 178–192.
- Gurtin, M.E., Weissmüller, J., Larché, F., 1998. A general theory for curved deformable interfaces in solids at equilibrium. *Philos. Mag.* A 78, 1093–1109.
- Hu, H.L., Chen, L.Q., 1997. Computer simulation of 90° degree ferroelectric domain formation in two-dimensions. *Mater. Sci. Eng. A* 238, 182–191.
- Huber, J.E., Fleck, N.A., Landis, C.M., McMeeking, R.M., 1999. A constitutive model for ferroelectric polycrystals. *J. Mech. Phys. Solids* 47, 1663–1697.
- Jona, F., Shirane, G., 1962. *Ferroelectric Crystals*. Pergamon Press, New York.

- Kessler, H., Balke, H., 2001. On the local and average energy release in polarization switching phenomena. *J. Mech. Phys. Solids* 49, 953–978.
- Landis, C.M., 2002a. A new finite-element formulation for electromechanical boundary value problems. *Int. J. Numer. Methods Eng.* 55, 613–628.
- Landis, C.M., 2002b. Fully coupled, multi-axial, symmetric constitutive laws for polycrystalline ferroelectric ceramics. *J. Mech. Phys. Solids* 50, 127–152.
- Landis, C.M., 2004. Energetically consistent boundary conditions for electromechanical fracture. *Int. J. Solids Struct.* 41, 6291–6315.
- Li, Y.L., Hu, S.Y., Liu, Z.K., Chen, L.Q., 2001. Phase-field model of domain structures in ferroelectric thin films. *Appl. Phys. Lett.* 78, 3878–3880.
- Li, Y.L., Hu, S.Y., Liu, Z.K., Chen, L.Q., 2002. Effect of substrate constraint on the stability and evolution of ferroelectric domain structures in thin films. *Acta Mater.* 50, 395–411.
- Li, Z., Chan, S.K., Grimsditch, M.H., Zouboulis, E.S., 1991. The elastic and electromechanical properties of tetragonal BaTiO₃ single crystals. *J. Appl. Phys.* 70, 7327–7332.
- McMeeking, R.M., Landis, C.M., 2005. Electrostatic forces and stored energy for deformable dielectric materials. *J. Appl. Mech.* 72, 581–590.
- Meyer, B., Vanderbilt, D., 2002. Ab initio study of ferroelectric domain walls in PbTiO₃. *Phys. Rev. B* 65, 104111.
- Nambu, S., Sagala, D.A., 1994. Domain formation and elastic long-range interaction in ferroelectric perovskites. *Phys. Rev. B* 50, 5838–5847.
- Nye, J.F., 1957. *Physical Properties of Crystals*. Oxford University Press, Great Britain.
- Pertsev, N.A., Zembilgotov, A.G., Tagantsev, A.K., 1998. Effect of mechanical boundary conditions on phase diagrams of epitaxial ferroelectric thin films. *Phys. Rev. Lett.* 80, 1988–1991.
- Provatas, N., Goldenfeld, N., Dantzig, J., 1998. Efficient computation of dendritic microstructures using adaptive mesh refinement. *Phys. Rev. Lett.* 80, 3308–3311.
- Shu, Y.C., Bhattacharya, K., 2001. Domain patterns and macroscopic behaviour of ferroelectric materials. *Philos. Mag. B* 81, 2021–2054.
- Toupin, R.A., 1956. The elastic dielectric. *J. Rational Mech. Anal.* 5, 849–914.
- Wang, J., Landis, C.M., 2004. On the fracture toughness of ferroelectric ceramics with electric field applied parallel to the crack front. *Acta Mater.* 52, 3435–3446.
- Wang, J., Shi, S.Q., Chen, L.Q., Li, Y., Zhang, T.Y., 2004. Phase field simulations of ferroelectric/ferroelastic polarization switching. *Acta Mater.* 52, 749–764.
- Warren, W.L., Dimos, D., Tuttle, B.A., Nasby, R.D., Pike, G.E., 1994. Electronic domain pinning in Pb(Zr,Ti)O₃ thin films and its role in fatigue. *Appl. Phys. Lett.* 65, 1018–1020.
- Xiao, Y., Shenoy, V.B., Bhattacharya, K., 2005. Depletion layers and domain walls in semiconducting ferroelectric thin films. *Phys. Rev. Lett.* 95, 247603.
- Xu, F., Trolrier-McKinstry, S., Ren, W., Xu, B., Xie, Z.-L., Hemker, K.J., 2005. Domain wall motion and its contribution to the dielectric and piezoelectric properties of lead zirconate titanate films. *J. Appl. Phys.* 89, 1336–1348.
- Zhang, W., Bhattacharya, K., 2005a. A computational model of ferroelectric domains. Part I: model formulation and domain switching. *Acta Mater.* 53, 185–198.
- Zhang, W., Bhattacharya, K., 2005b. A computational model of ferroelectric domains. Part II: grain boundaries and defect pinning. *Acta Mater.* 53, 199–209.